

Universality of electronic characteristics and photocatalyst applications in the two-dimensional Janus transition metal dichalcogenides

Congxin Xia,^{1,*} Wenqi Xiong,¹ Juan Du,¹ Tianxing Wang,¹ Yuting Peng,² and Jingbo Li³

¹College of Physics and Materials Science, Henan Normal University, Xinxiang 453007, China

²Department of Physics, University of Texas at Arlington, Arlington, Texas 76019, USA

³Institute of Semiconductors, Chinese Academy of Sciences, Beijing 100083, China



(Received 9 July 2018; revised manuscript received 27 August 2018; published 17 October 2018)

Due to mirror symmetry breaking, two-dimensional Janus transition metal dichalcogenides MXY ($M = \text{Mo, W}$; $X, Y = \text{S, Se, Te}$) present charming electronic properties. However, there have not been many related studies as of yet, and the intrinsic physical pictures are unclear. Here, we use first-principles calculations to explore the universality of electronic characteristics and photocatalyst applications of Janus MXY , finding that the induced dipole moment, vibrational frequency, Rashba parameters, and direct-indirect band transition of monolayer MXY are deeply associated with the atomic radius and electronegativity differences of chalcogen X and Y elements. The internal electric field renders Janus MXY the ideal photocatalysts. Moreover, the stacking-dependent on/off switch of the dipole moment further confirms that asymmetric Janus MXY serves as a promising candidate for highly efficient photocatalysts within a broad range from infrared, visible, to ultraviolet light.

DOI: [10.1103/PhysRevB.98.165424](https://doi.org/10.1103/PhysRevB.98.165424)

I. INTRODUCTION

The discovery of graphene has motivated people to explore new two-dimensional (2D) materials due to their novel properties [1–5]. In particular, monolayer transition metal dichalcogenides (TMDC) MX_2 ($M = \text{Mo, W}$; $X = \text{S, Se, Te}$) have direct band structures, suitable gap values (approximately 1.0–2.0 eV), high carrier mobility ($> 200 \text{ cm}^2 \text{ V}^{-1} \text{ s}^{-1}$), and high ambient stability [6–8], which make them ideal materials for optoelectronic devices such as photodetectors and field-effect transistors (FETs) [9,10]. Additionally, TMDCs also exhibit unconventional physics phenomena, e.g., strong coupling between spin and valley degrees of freedom [6,11–13]. However, TMDCs still lack Rashba spin-orbit coupling (SOC) and electric-controlled spin precession, which hinders their potential applications in spin FETs.

More recently, through chemical vapor deposition (CVD), the polar Janus MXY ($M = \text{Mo, W}$; $X, Y = \text{S, Se, Te}$) monolayer has been successfully synthesized by sulfurization in MoSe_2 or selenization in MoS_2 [14,15]. Thus, the space group D_{3h} of $2\text{H } MX_2$ is also changed to C_{3v} for Janus MXY [16–18]. Moreover, Cheng *et al.* found that polar MXY presents SOC-induced Rashba spin splitting [19]. Yao *et al.* also reported that monolayer WSeTe has a large Rashba spin parameter of 0.92 eV \AA , which is much larger than the values of traditional heterostructures [20]. The giant Rashba SOC renders Janus MXY a promising candidate for future spintronic devices.

In addition, it is well known that a highly efficient water-splitting photocatalyst requires two fundamental elements: (i) an appropriate band gap to straddling the reduction

potential (-4.44 eV) and the oxidation potential (-5.67 eV); (ii) effective separation of electrons and holes [21,22]. However, in recent studies Janus MXY created a dipole moment-induced internal electric field [16,19], which indicates that the internal electric field can induce a bend of the energy level and a separation of electron-hole pairs. Thus, the traditional water splitting mechanism may be broken in polar Janus MXY [23–25].

In this work, we will present systematic studies on the intrinsic physics properties of Janus MXY using the first-principles method. We explore the universality of structural parameters, phonon vibrations, and electronic properties with respect to the atomic species. Moreover, the optical absorption and water splitting activities indicate that Janus MXY could be considered as an ideal photocatalyst.

II. CALCULATION METHOD

For the electronic structure calculation of all considered Janus MXY materials, we use the Vienna Ab initio Simulation Package (VASP) code based the density functional theory (DFT) [26]. The generalized gradient approximation (GGA) and projected augmented wave (PAW) are used to treat the exchange correlation potential and ion-electron interaction [27,28]. Due to the existence of dipole moment in Janus MXY materials, the dipole correction is introduced. Also, during the calculations, the kinetic energy cutoff of the plane wave and the k -point meshes of the Brillouin zone (BZ) are set to 500 eV and $15 \times 15 \times 1$ [29], respectively. To avoid the periodic interaction, a vacuum layer thickness of 20 \AA is added. Moreover, the geometric convergence criteria for energy and forces are set at 10^{-5} eV and 0.01 eV/\AA , respectively. The van der Waals (vdW) interlayer interaction is considered by

*xiacongxin@htu.edu.cn

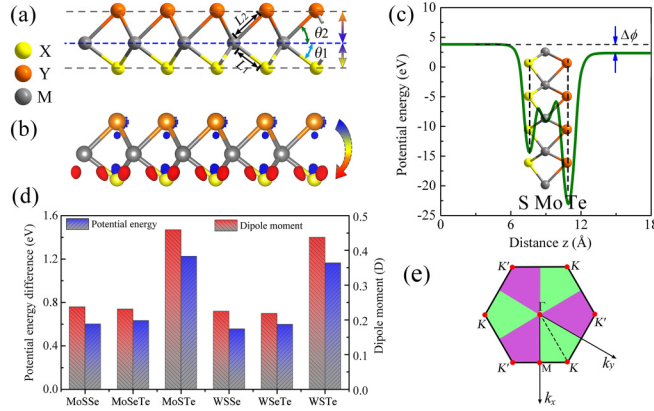


FIG. 1. (a) The atomic structure of monolayer Janus MXY . (b) The charge density difference of monolayer MoSTe with an isovalue of $0.02 e/\text{\AA}^3$. The arrow marks the direction of the net electric field. Red and blue denote electron accumulation and depletion, respectively. (c) Planar average electrostatic potential energy of the monolayer MoSTe. $\Delta\phi$ is the potential energy difference. (d) The potential energy difference and dipole moment of monolayer Janus MXY . (e) The first BZ of Janus MXY .

using a semiempirical DFT-D2 method [30,31]. The spin-orbit coupling (SOC) effect is included in the self-consistent calculations. In addition, the hybrid Heyd-Scuseria-Ernzerhof (HSE) method is used to correct the band structures [32].

The PHONOPY code is used to confirm the thermal stability and obtain the phonon vibration modes of monolayer Janus MXY [33,34]. Based on the density functional perturbation theory (DFPT) [35], the atomic displacements are treated as a perturbation potential. We construct the 5×5 MXY supercell and adopt the 5×5 k -point meshes to create accurate force constants, the dynamical matrix, and the phonon spectrum.

The thermal stability of Janus MXY at room temperature is examined by *ab initio* molecular dynamics (MD) simulation [36,37]. And the constant particle number, volume, and temperature (NVT) ensemble are simulated by adopting the algorithm of Nose. The test sample is chosen as a 6×6 supercell, and the total time and time step are set as 5×10^{-12} and 1×10^{-15} s, respectively.

To evaluate the excitonic properties of the Janus MXY monolayer, the quasiparticle energy is calculated within the GW method. We use the $15 \times 15 \times 1$ k -meshes to obtain the accurate band structures through the WANNIER90 program [38], and the exciton effect are calculated by solving the Bethe-Salpeter equation (BSE) [39,40].

TABLE I. Calculated lattice constants (a and b), bond length (d_{M-X}) and (d_{M-Y}), bond length difference (Δd_{X-Y}), the angle (θ_1 and θ_2), cohesive energy (E_{coh}), potential energy difference ($\Delta\phi$) and dipole moment (μ) of monolayer Janus MXY .

Pattern	$a = b$ (\AA)	d_{M-X} (\AA)	d_{M-Y} (\AA)	Δd_{X-Y} (\AA)	θ_1 (deg)	θ_2 (deg)	$\Delta\theta$ (deg)	E_{coh} (eV)	$\Delta\phi$ (eV)	μ (D)
MoSSe	3.250	1.528	1.704	0.176	39.2	42.2	3	2.44	0.76	0.188
MoSeTe	3.433	1.615	1.863	0.248	39.2	43.2	4	1.37	0.74	0.198
MoSTe	3.364	1.472	1.901	0.429	37.2	44.4	7.2	1.65	1.47	0.383
WSSe	3.247	1.535	1.713	0.178	39.3	42.4	3.1	2.17	0.72	0.174
WSeTe	3.432	1.623	1.870	0.247	39.3	43.3	4	0.86	0.7	0.187
WSTe	3.361	1.478	1.909	0.431	37.3	44.5	7.2	1.23	1.40	0.364

III. RESULTS AND DISCUSSIONS

A. Structure, stability, and phonon dispersion of monolayer MXY

Figure 1(a) shows the atomic structure of Janus MXY monolayer, in which we define the atomic radius of the X atom as always smaller than that of the Y atom. Compared with the space group D_{3h} of $2H-MX_2$, the space group of monolayer MXY is changed to C_{3v} due to mirror symmetry breaking. After the structural optimization, Table I shows the calculated structural parameters, including lattice constants, bond lengths, and angles. The related results are also plotted in Fig. S1 (see the supplemental material [41]), which reveals the following trends:

(i) As the XY atomic radius sum increases (SSe \rightarrow STe \rightarrow SeTe), the lattice constants of MXY materials linearly increase.

(ii) The difference of bond lengths (d_{M-X} and d_{M-Y}) and angles (θ_1 and θ_2) is directly proportional to the XY atomic radius difference (SSe \rightarrow SeTe \rightarrow STe).

In Fig. 1, we further investigate the mirror-symmetry-breaking-induced dipole moments of Janus MXY . As an example, Fig. 1(b) plots the charge density difference of the MoSTe monolayer. It can be seen that the electron aggregation and depletion occur at S and Te atoms, respectively, which are attributed to different atom electronegativity: S (2.58) and Te (2.10). Thus, the charge redistribution can induce the net electric field and dipole moment pointing from Te to S in the MoSTe monolayer. Meanwhile, Fig. 1(c) shows that MoSTe has an electrostatic potential difference $\Delta\phi$ and a higher potential at the S atom side. Moreover, in Fig. 1(d) we also display the potential energy difference and dipole moment for the Janus MXY materials. Obviously, the potential energy difference is proportional to the dipole moment. Due to the large electronegativity difference of S and Te atoms, the MSTe material has the largest dipole moments, which are nearly double those of MSSe and MSeTe.

In the Janus MXY materials, the bonds between M and X (Y) atoms have covalent character. To assess the strength of covalent bonds, we calculate the cohesive energy of MXY by using the following equation:

$$E_{\text{coh}} = \mu_M - \mu_X - \mu_Y - E_{\text{tot}}, \quad (1)$$

where μ_M , μ_X , and μ_Y are the chemical energies of M , X , and Y atoms, respectively. E_{tot} is the total energy of monolayer MXY . The related results are given in Fig. S1(d) and Table I, showing that the cohesive energies decrease as the sum of the

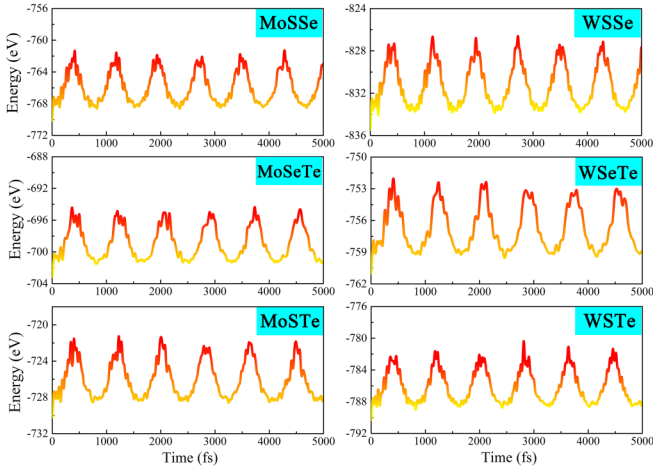


FIG. 2. The total energies of Janus MXY as a function of the time under the molecular dynamics simulations at 300 K.

X and Y atomic radii increases ($S\text{Se} \rightarrow \text{STe} \rightarrow \text{SeTe}$) (see the supplemental material [41]). Thus, Janus MSSe materials are energetically most favorable with the largest cohesive energies among Janus MXY .

Meanwhile, the thermal stability of Janus MXY is qualitatively tested by MD simulation at room temperature. Figure 2 showed the fluctuations of total energies for the MXY monolayer, indicating the total energy oscillation persistently remains at a fixed value. Moreover, Fig. S2 displays that after the MD simulation, there is no bond-breaking and structural distortion in the final configurations of the MXY monolayer (see the supplemental material [41]). These results imply that the Janus MXY materials can be experimentally feasible at room temperature.

To further discuss the structural stability and phonon vibration modes of Janus MXY , Fig. 3 shows that the phonon dispersion of MXY has nine branches, including six optical and three acoustic branches. Moreover, the three acoustic branches have lower frequency and contain in-plane longitudinal

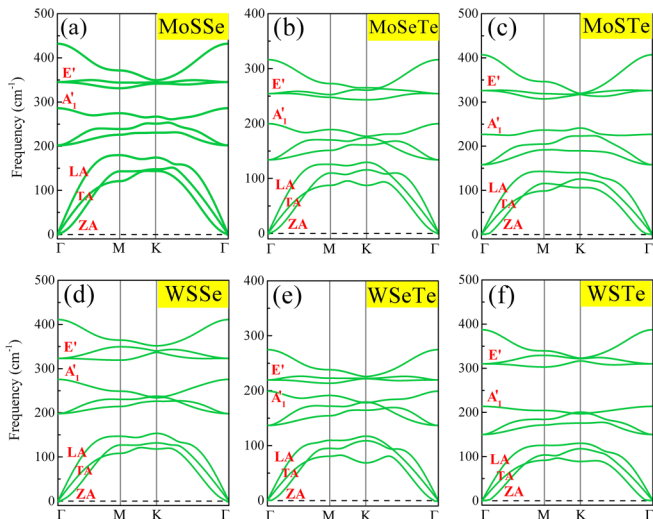


FIG. 3. The phonon dispersion of monolayer (a) MoSSe, (b) MoSeTe, (c) MoSTe, (d) WSSe, (e) WSeTe, and (f) WSTe.

TABLE II. The vibration frequencies of monolayer MXY and MX_2 .

	MoSSe	MoSeTe	MoSTe	WSSe	WSeTe	WSTe
A'_1 (cm^{-1})	286	200	227	276	199	214
E' (cm^{-1})	345	255	326	323	220	310
	MoS ₂	MoSe ₂	MoTe ₂	WS ₂	WSe ₂	WTe ₂
A'_1 (cm^{-1})	402	237	170	412	244	175
	403 [39]	241 [40]	171 [42]	418 [41]	250 [43]	179 [44]
E' (cm^{-1})	378	279	230	348	240	192
	384 [39]	[40]	[42]	356 [41]	248 [43]	198 [44]

nal acoustic (LA), transverse acoustic (TA), and out-of-plane acoustic (ZA) modes. For six optical branches, it consists of two in-plane longitudinal optical (LO_1 and LO_2), two in-plane transverse optical (TO_1 and TO_2), and two out-of-plane optical (ZO_1 and ZO_2) modes. Based on the irreducible representations at the Γ point, the six optical modes are classified as degenerate E' (LO_2 and TO_2) and E'' (LO_1 and TO_1) and nondegenerate A'_1 (ZO_1) and A'_2 (ZO_2). Figure 3 shows that there is no negative acoustic branch found at phonon spectra around the Γ point, which implies that the monolayer Janus MXY could be favorably stable.

For the characteristics of the phonon spectrum, Table II summarizes the vibration frequencies of A'_1 and E' modes from Fig. 3. We see that for the MoSSe monolayer, the calculated out-of-plane A'_1 and in-plane E' modes are 286 and 345 cm^{-1} , agreeing well with the Raman peaks of 287 and 355 cm^{-1} [14,15]. Moreover, the frequencies of the A'_1 and E' modes are inversely proportional to the sum of the M , X , and Y atomic radii. Therefore, we find that for the MoSSe monolayer, the sum of the Mo, S, and Se atomic radii is smallest, and thus it has the largest frequencies of A'_1 and E' modes. Additionally, in Fig. S3, we also calculate the phonon dispersion of MX_2 and summarize its vibration modes in Table II, which are consistent with previous results [42–47]. It can be seen that compared with the MX_2 monolayer, the vibration modes A'_1 and E' have a frequency shift in the Janus MXY monolayer. The shifts of out-of-plane A'_1 and in-plane E' peaks are mainly attributed to the change of lattice constant and out-of-plane symmetry-breaking, respectively.

B. Electronic properties of monolayer MXY

Now we study the electronic characteristics of the Janus MXY monolayer. In Fig. 4, we present the band structures of Janus MXY considering the SOC interaction. The results show that monolayer MSSe and MSeTe have direct band structures because their conduction-band minimum (CBM) and valence-band maximum (VBM) are located at the same K point. However, the CBM and VBM of monolayer MSTe lie at the K and Γ points, respectively, inducing the indirect band structures in Janus MSTe. These behaviors are different from the direct band structures of monolayer MX_2 [6]. Additionally, to support our calculated results, Fig. S4 also shows the calculated band structures of monolayer MXY using Perdew-Burke-Ernzerhof (PBE) and HSE methods, and the SOC effects are not considered. It can be found that the SOC interaction and calculation methods only decrease the

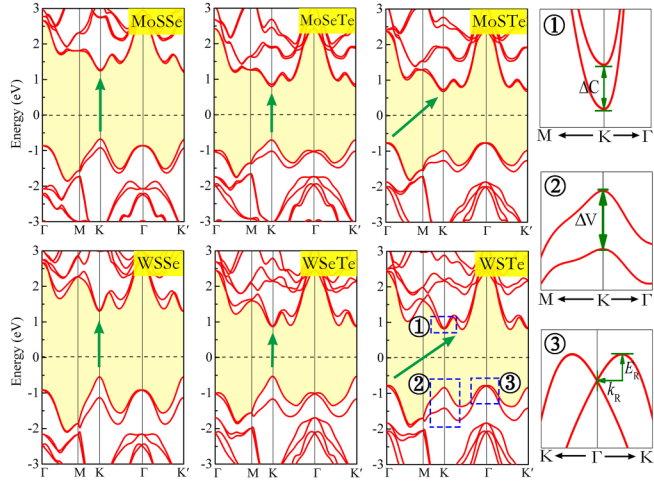


FIG. 4. The band structures of monolayer Janus MXY are given by HSE and SOC methods. The insets denote an enlarged view of the band structures.

band-gap values while maintaining the band-structure types (direct or indirect).

Moreover, Fig. S5 summarizes the gap values of MXY and MX_2 obtained using the HSE method, and it is found that the order of band-gap values is $MS_2 > MSSe > MSe_2 > MSeTe > MSTe > MTe_2$. Thus, we can conclude that the band-gap values of 2H MX_2 can be modulated by forming Janus MXY structures. The modulation strategy is similar to the alloy doping in MX_2 [48–50], which provides a rational design for tunable optoelectronic properties of the 2D TMDC materials.

Table III reveals that the SOC splitting at the VBM is one or two orders of magnitude higher than that at the CBM. Due to the heavier metal atoms, the VBM of WXY has larger SOC splitting than that of $MoXY$ and reaches nearly 640 meV. Meanwhile, we also observe the d_{z^2} orbital-involved Rashba spin splitting in the MXY materials. To calculate the Rashba parameter $\alpha_R = 2E_R/k_R$ [19], Fig. 4 shows the magnified Rashba energy E_R and momentum offset k_R at the Γ point. The related results are summarized in Table III, which illustrates that the parameters E_R , k_R , and α_R are directly proportional to the sum of X and Y atomic radii. Particularly, the Rashba coupling parameter α_R of MoSeTe and WSeTe exceeds 1.3 eV \AA , which is much larger than that of tradi-

tional heterostructures InGaAs/InAlAs and LaAlO₃/SrTiO₃ [51,52]. The Janus MXY with large Rashba spin splitting is expected to stabilize spin, which is desired in spintronics devices.

To gain more insight into the orbital contribution of band structures, Fig. S6 shows the d orbital-resolved projected band structures. We can find that for monolayer MXY , the electronic states near the CBM and the VBM mainly stem from the d orbitals of transition metal atoms, which are similar to previous studies on MX_2 . Also, Fig. S6 shows that for Janus MXY , the highest (lowest) valence (conduction) band at K originates from the $d_{xy} + d_{x^2-y^2}$ (d_{z^2}) orbital. The strong hybridization between d_{xy} and $d_{x^2-y^2}$ orbitals of M atoms also causes the large SOC splitting of the VBM at the K point. For the highest valence band at Γ , the electronic states are attributed to the d_{z^2} orbital. However, the $d_{yz} + d_{xz}$ orbital appears at a deep energy level above and below the Fermi level 2 eV, which does not directly involve into the interplay near the CBM and the VBM.

To estimate the exciton binding energy of the Janus MXY monolayer, Fig. S7 plots the band structures obtained using GW methods, and Fig. S8 presents the absorption spectrum obtained by the $GW+BSE$ methods. Moreover, the exciton binding energy is defined as the difference between the GW band gap and the first absorption peak of the $GW+BSE$ absorption spectrum. Thus, we can calculate the exciton binding energy of the Janus MXY monolayer, and the related values are summarized in Table III. It can be seen that the scaling values of exciton binding energies range from 0.308 to 0.469 eV, which are a little lower than that of the conventional 2H MX_2 range from 0.47 to 0.55 eV [53], which results from the internal electric field in the 2D Janus MXY material. In addition, it is well known that exciton states are formed via the electron-hole Coulomb interaction. Thus, compared to MX_2 , the Janus MXY materials have smaller exciton binding energy, which are ideal for photocatalysis because of the effective separation of electron-hole pairs in these materials.

Next we calculate the high-frequency dielectric constants ϵ_∞ via density functional perturbation theory (DFPT). To verify the rationality of this model, we first take monolayer MoS₂ as a sample and calculate its high-frequency dielectric functional ϵ_∞ . The obtained value of 4.66 is consistent with reported values of 4.44 and 5.00 [54,55]. Then, the high-frequency dielectric constants ϵ_∞ of Janus MXY are listed in Table III, implying that the ϵ_∞ is proportional to the sum of XY atomic radii.

TABLE III. The conduction and valence band splitting (Δ_C and Δ_V), obtained band gap from PBE (E_g^{PBE}), HSE methodS without SOC (E_g^{HSE}) and with SOC ($E_g^{\text{HSE+SOC}}$), the Rashba energy E_R , momentum offset k_R , Rashba parameter α_R , exciton binding energy (E_{bind}) and high-frequency dielectric constant (ϵ_∞) for monolayer Janus MXY .

Pattern	Δ_C (meV)	Δ_V (meV)	E_g^{PBE} (eV)	E_g^{HSE} (eV)	$E_g^{\text{HSE+SOC}}$ (eV)	E_R (meV)	k_R (\AA^{-1})	α_R (eV \AA)	E_{bind} (meV)	ϵ_∞
MoSSe	34	246	1.56	2.01	1.98	1.4	0.012	0.239	0.426	4.93
MoSeTe	61	314	1.27	1.71	1.51	35.8	0.052	1.382	0.469	5.78
MoSTe	53	282	1.02	1.47	1.45	4.2	0.019	0.44	0.447	5.73
WSSe	25	584	1.70	2.18	1.85	3.9	0.016	0.5	0.347	4.54
WSeTe	9	637	1.35	1.79	1.40	29.4	0.041	1.434	0.308	5.38
WSTe	7	579	1.23	1.71	1.60	10.7	0.023	0.93	0.431	5.25

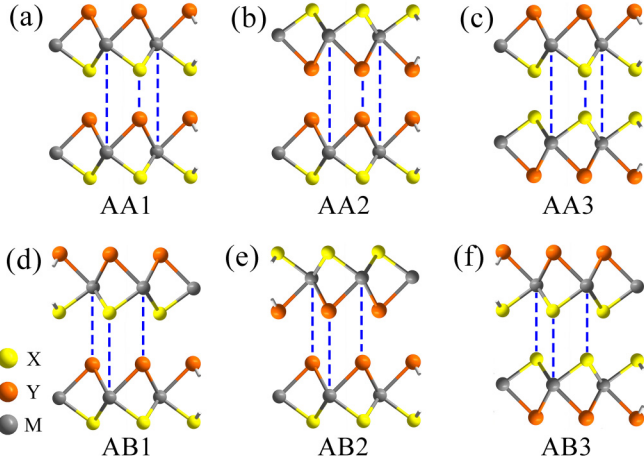


FIG. 5. The atomic structures of bilayer MXY with different stacking models (a) AA1, (b) AA2, (c) AA3, (d) AB1, (e) AB2, and (f) AB3.

For the 2D semiconductor systems, the carrier mobility μ can be evaluated by deformation theory on the basis of the effective-mass approximation [56], which is expressed as

$$\mu = \frac{2e\hbar^3 C}{3k_B T |m^*|^2 E_1^2}, \quad (2)$$

where $C = [\partial^2 E / \partial \delta^2] / S^0$ is the elastic modulus, in which E is the total energy, δ is the applied uniaxial strain, and S^0 is the area of the MXY . The $m^* = \hbar^2 (\partial^2 E / \partial k^2)^{-1}$ is the effective mass of the electron or hole (\hbar is Planck's constant and k is the wave vector in momentum space). E_1 is defined as $E_1 = \Delta E / (\Delta l / l_0)$, in which ΔE is the band-edge shift with respect to the lattice change. And the k_B and T are the Boltzmann constant and temperature (300 K), respectively. During the calculations, we build the rectangle supercell and apply the uniaxial strain. Table S2 presents the mobility of the electron and hole under room temperature. It can be seen that the carrier mobility along the x and y directions is not exactly equal, implying a slightly anisotropic feature. Moreover, the carrier mobility of WSSe is larger than that of MoSSe due to the larger elastic modulus and smaller effective mass. Especially for WSSe, it has the highest hole mobility of $627 \text{ cm}^2 \text{ V}^{-1} \text{ s}^{-1}$. However, for the WSTe and MoSTe cases, they have lower hole mobility because of a larger hole effective mass.

C. Structural and electronic properties of bilayer MXY

Here, we investigate the characteristics of the Janus MXY bilayer. Figure 5 depicts six kinds of MXY bilayer stacking models, denoted AA_n and AB_n ($n = 1, 2, 3$). For AA_n (AB_n) stacking, the XY atom lies over the XY (M) atom, while the M atom is located over the (M) XY atom. Meanwhile, $AB1$ stacking is obtained by rotating each layer 180° in $AA1$ stacking. Reversing each layer in $AA1$ ($AB1$) stacking can form $AA2$ and $AA3$ ($AB2$ and $AB3$). In the $AA2$ and $AB2$ ($AA3$ and $AB3$) stacking models, two Y (X) atom layers are combined face to face. Moreover, the point groups of $AA1$, $AA2$, $AA3$, $AB1$, $AB2$, and $AB3$ stacking models

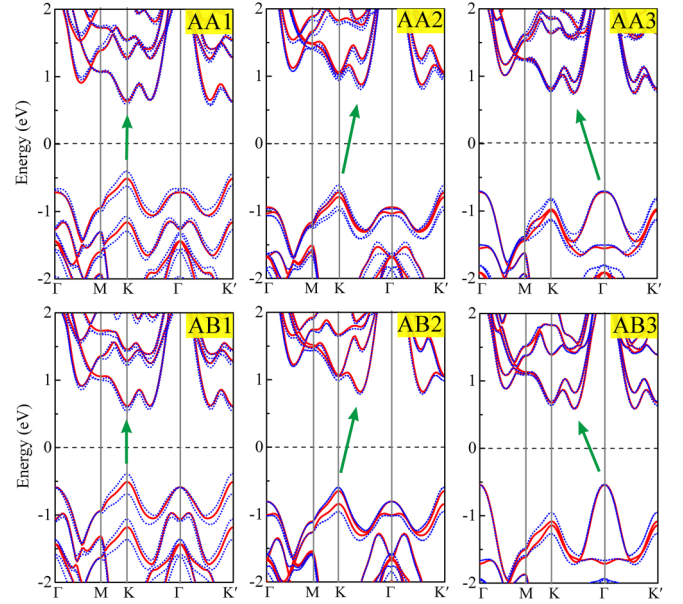


FIG. 6. The band structures of bilayer MoSeTe with various stacking models are given by HSE (red solid line) and HSE+SOC (blue dashed line) methods.

are C_{3v} , D_{3h} , D_{3h} , C_{3v} , D_{3d} , and D_{3d} , respectively. Thus, in the following, we will further study the stacking-dependent stability, dipole moment, and electronic properties of bilayer MXY materials.

First, we calculate the binding energy of bilayer MXY based on the equation

$$E_b = 2E_{\text{monolayer}} - E_{\text{bilayer}}, \quad (3)$$

where the $E_{\text{monolayer}}$ and E_{bilayer} are the total energies of monolayer and bilayer MXY , respectively. It can be seen from Table S1 that all bilayer models are energetically stable. The AB_n pattern has a larger binding energy than that of AA_n stacking, and $AB2$ stacking MXY has the largest binding energy among all stacking models.

Then we investigate the stacking effects on the internal electric field and dipole moment of the Janus MXY bilayer. Taking the MoSTe bilayer as an example, Fig. S9 plots the planar average electrostatic potential of AA_n and AB_n stacking patterns. We can see that $AA1$ and $AB1$ models have the electrostatic potential difference $\Delta\phi$. However, for $AA2$, $AA3$, $AB2$, and $AB3$ patterns, the $\Delta\phi$ becomes zero because they heal the out-of-plane symmetry breaking in monolayer form. Moreover, Table S1 shows that the potential difference $\Delta\phi$ of $AA1$ and $AB1$ is nearly the same, implying that the net electric field is immune to the in-plane rotation. Moreover, the potential difference and dipole moments of $AA1$ and $AB1$ are almost double that of the MXY monolayer due to the out-of-plane asymmetric stacking.

To study the electronic properties of the MXY bilayer, Fig. 6 plots the band structures of bilayer MoSeTe with various stacking models. For $AA1$ and $AB1$ models, the CBM and VBM are still located at the K point, indicating they possess the characteristics of direct band structures. However, the $AA2$, $AA3$, $AB2$, and $AB3$ models form the indirect band structures. In particular, $AA3$ and $AB3$ models can

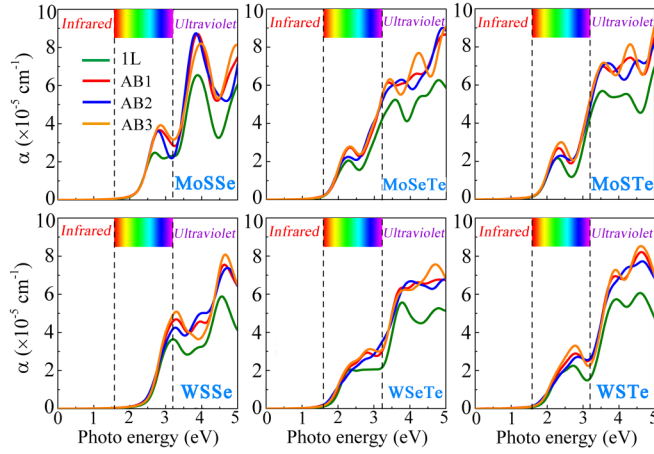


FIG. 7. Optical absorption coefficients of monolayer (1L), bilayer $AB1$, $AB2$, and $AB3$ MXY calculated by the HSE+SOC method.

pull down the VBM at the K point, inducing the direct-indirect gap transition. Moreover, Table S1 shows that the high-symmetry stacking effectively tunes the band-gap values of bilayer MoSeTe from 1.46 eV (1.6 eV) to 0.93 eV (1.12 eV) with (without) the SOC interaction. In addition, another Janus MXY bilayer also presents the stacking-dependent band-gap values.

To analyze the high-symmetry stacking effect, Fig. S10 plots d orbital-resolved projected band structures of bilayer MoSeTe. Compared with the MoSeTe monolayer in Fig. S6, the bilayer stacking makes no difference to the d orbital dispersion at the first BZ. The d_{z^2} orbital dominates the lowest conduction band at K and the highest valence band at Γ , while the orbital dominates the highest valence band at K . For $AA1$ and $AB1$ models, the out-of-plane asymmetry breaks the conduction-band (d_{z^2}) and valence-band ($d_{xy} + d_{x^2-y^2}$) degeneracy at K . However, the $AA2$, $AA3$, $AB2$, and $AB3$ models recover the out-of-plane symmetry and degeneracy band at K .

D. Optical properties

To examine the stacking effects on the optical properties of Janus MXY , we calculate the absorption coefficients $\alpha(E)$ through the equation

$$\alpha(E) = \frac{4\pi E}{hc} \sqrt{0.5((\varepsilon_1^2 + \varepsilon_2^2)^{0.5} - \varepsilon_1)}, \quad (4)$$

where ε_1 and ε_2 are the real and imaginary parts of the dielectric function [57], respectively. Figure 7 presents the optical absorption coefficients for monolayer, bilayer $AB1$, $AB2$, and $AB3$ MXY materials. We find that the Janus MXY allows the high absorption coefficients (approximately 10^5 cm^{-1}) and broad wavelength range of optical absorption from near-infrared to ultraviolet. For all MXY materials, the absorption coefficients of the MXY bilayer have larger values than that of the MXY monolayer, indicating the optical absorption of the MXY bilayer is remarkably enhanced under the visible and ultraviolet light ranges. The strong visible and ultraviolet light

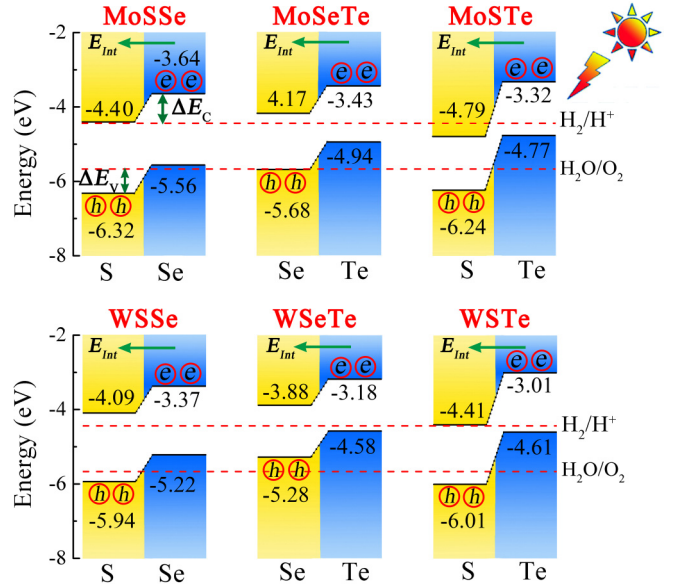
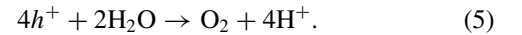


FIG. 8. Band alignments of monolayer Janus MXY with respect to the redox potentials of water. E_{int} denotes the internal electric field.

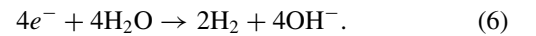
absorption will provide obvious advantage for Janus MXY as the ideal photocatalyst.

E. Photocatalyst

To further check the possible applications of Janus MXY in the photocatalyst, Fig. 8 plots the band alignments of the Janus MXY monolayer with respect to the redox potential of water using the HSE+SOC method. On the X atom layer side, the VBM is lower than the oxidation potential (-5.67 eV) by ΔE_V , indicating that the holes are readily transferred from the VBM to H_2O and oxidize it to O_2 :



On the Y atom layer side, when the CBM is higher than the reduction potential (-4.44 eV) by ΔE_C , the electrons can flow to H_2O and catalyze it to H_2 :



Meanwhile, the dipole moment-induced internal electric field spontaneously separates photo-generated electrons and holes, and localizes the holes and electrons on both the X and Y sides, respectively.

The photocatalytic ability of Janus MXY is evaluated as follows. The photocatalyst absorbs solar energy to convert energy into H_2 and O_2 . Moreover, the kinetic overpotentials (ΔE_C and ΔE_V) are needed to drive the redox reaction. Table S3 gives the potential difference ΔE_C (ΔE_V) between the CBM (VBM) and the reduction potential (oxidation potential). Compared with the potentials of H^+/H_2 and $\text{H}_2\text{O}/\text{O}_2$, the WSeTe monolayer has enough ΔE_C of 1.26 eV to produce H_2 , while its potential of the VBM fails in producing oxygen. However, the other five materials have enough energy difference (ΔE_C and ΔE_V) from 0.01 to 1.43 eV to achieve water splitting. In particular, the MSTe materials have the largest dipole moments and electrostatic potentials, which induce the electron and hole to be separated effectively and create

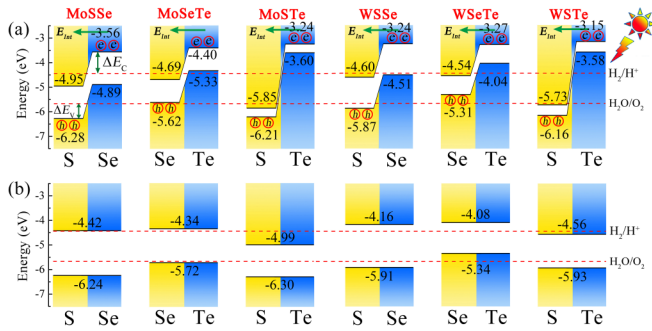


FIG. 9. Band alignments of bilayer Janus MXY for (a) $AB1$ and (b) $AB2$ stacking models with respect to the redox potentials of water. The E_{int} denotes the internal electric field.

larger ΔE_C and ΔE_V . Generally, the photocatalytic efficiency is proportional to the potential difference between the CBM (VBM) and the reduction (oxidation) potential and the numbers of electrons and holes. Therefore, the $MSTe$ materials can be proposed as the more preferred photocatalysts under the broad range from near-infrared, visible, to ultraviolet light because they have a larger potential than the reduction/oxidation potential and a stronger internal electric field.

According to the above studies on the values of dipole moments, the MXY bilayer can be classified into two types: $AA1$ and $AB1$; $AA2$, $AA3$, $AB2$, and $AB3$ patterns. The former type has almost a double dipole moment of the MXY monolayer, while the latter type has a zero dipole moment. Thus, we select $AB1$ and $AB2$ stacking models as the target materials, and we study their photocatalytic ability in Fig. 9. Moreover, for the $AB1$ stacking, Table S3 shows that bilayer $MoSSe$, $MoSTe$, $WSSe$, and $WSTe$ have a large potential difference ΔE_C and ΔE_V for the reduction and oxidation reaction. The bilayer $MoSeTe$ and $WSeTe$ with $AB1$ stacking have large ΔE_C to achieve H_2 reduction, while their VBM is higher than the oxidation potential and fails to produce O_2 .

However, the $AB2$ stacking models are compelled to conform to the conventional photocatalytic rule due to the zero dipole moment, and the water reduction and oxidation potentials must lie between the CBM and the VBM. It can be seen that only $MoSSe$, $MoSeTe$, and $WSSe$ with $AB2$ stacking are strictly compliant with this rule. Although they meet the basic requirement, the potential differences ΔE_C and ΔE_V are smaller than 0.6 eV, which will present very low efficiency in splitting water. Moreover, $MoSTe$, $WSeTe$, and $WSTe$ with $AB2$ stacking are even harmful to the redox reaction. Therefore, the recovering of out-of-plane symmetry in the MXY bilayer may not be beneficial to the water splitting. Based on the strength of the dipole moment and the internal electric field, the $AA1$ and $AB1$ MXY bilayer,

especially $MSTe$, can be proposed as the high-efficiency and broad wavelength photocatalysts for water splitting from near-infrared, visible, to ultraviolet light.

It should be noted that in this work, we only consider the redox potentials of H^+/H_2 and H_2O/O_2 at an aqueous solution $pH = 0$. Meanwhile, the water splitting efficiency is closely related to the aqueous solution pH . According to the Nernst equation [58–60], water redox potentials at room temperature vary as a function of the pH ,

$$E^{pH} = E^{pH=0} - 0.059 \times pH, \quad (7)$$

where E^{pH} is the redox potential. Using this equation, we can obtain the redox potentials of H^+/H_2 and H_2O/O_2 for any pH . As the pH value increases from 0 to 14, the corresponding redox potentials (H^+/H_2 and H_2O/O_2) will shift upward. The kinetic overpotential ΔE_C (ΔE_V) is the difference between the CBM (VBM) and the reduction (oxidation) potential. If the redox potentials of H^+/H_2 and H_2O/O_2 lie between the CBM and the VBM, the rise of pH will decrease (increase) overpotential ΔE_C (ΔE_V). For monolayer $WSTe$, it is capable of producing H_2 and O_2 from an aqueous solution with $pH > 5.8$. Therefore, Janus MXY presents the aqueous solution pH -related water splitting efficiency.

IV. CONCLUSIONS

In summary, we investigated theoretically the structural stability, phonon vibration, band structures, carrier mobility, exciton states, optical absorption, and photocatalyst properties of 2D Janus MXY materials, and we explored the relationship between the intrinsic physics mechanisms and structure parameters. The dipole moment, vibrational frequency, Rashba parameters, and direct-indirect band transition of monolayer MXY are deeply associated with the atomic radius and electronegativity differences of chalcogen X and Y elements. The internal electric field facilitate Janus MXY to become ideal photocatalysts because of the separation of electron-hole pairs and the bending of energy levels. Moreover, the stacking-dependent on/off switch of the dipole moment further confirms that asymmetric Janus MXY serves as a promising candidate for highly efficient photocatalysts within a broad range from infrared, visible, to ultraviolet light.

ACKNOWLEDGMENTS

This research was supported by the National Natural Science Foundation of China (No. 11674084), Henan Natural Science Foundation (No. 162300410169), and Science Technology Innovation Talents in Universities of Henan Province (Grant No. 18HASTIT029). The calculations are also supported by The High Performance Computing Center of Henan Normal University.

- [1] K. S. Novoselov, A. K. Geim, S. V. Morozov, D. Jiang, M. I. Katsnelson, I. V. Grigorieva, S. V. Dubonos, and A. A. Firsov, *Nature (London)* **438**, 197 (2005).
- [2] R. R. Nair, P. Blake, A. N. Grigorenko, K. S. Novoselov, T. J. Booth, T. Stauber, N. M. R. Peres, and A. K. Geim, *Science* **320**, 1308 (2008).

- [3] Y. Zhang, Y.-W. Tan, H. L. Stormer, and P. Kim, *Nature (London)* **438**, 201 (2005).
- [4] Q. H. Wang, K. Kalantar-Zadeh, A. Kis, J. N. Coleman, and M. S. Strano, *Nat. Nanotech.* **7**, 699 (2012).
- [5] J. Kang, S. Tongay, J. Zhou, J. Li, and J. Wu, *Appl. Phys. Lett.* **102**, 012111 (2013).

- [6] A. Kuc and T. Heine, *Chem. Soc. Rev.* **44**, 2603 (2015).
- [7] X. Zhang, X.-F. Qiao, W. Shi, J.-B. Wu, D.-S. Jiang, and P.-H. Tan, *Chem. Soc. Rev.* **44**, 2757 (2015).
- [8] W. S. Yun, S. W. Han, S. C. Hong, I. G. Kim, and J. D. Lee, *Phys. Rev. B* **85**, 033305 (2012).
- [9] Y. Xie, B. Zhang, S. Wang, D. Wang, A. Wang, Z. Wang, H. Yu, H. Zhang, Y. Chen, M. Zhao, B. Huang, L. Mei, and J. Wang, *Adv. Mater.* **29**, 1605972 (2017).
- [10] Z. Yin, H. Li, H. Li, L. Jiang, Y. Shi, Y. Sun, G. Lu, Q. Zhang, X. Chen, and H. Zhang, *ACS Nano* **6**, 74 (2012).
- [11] Z. Y. Zhu, Y. C. Cheng, and U. Schwingenschlöggl, *Phys. Rev. B* **84**, 153402 (2011).
- [12] D. Xiao, G.-B. Liu, W. Feng, X. Xu, and W. Yao, *Phys. Rev. Lett.* **108**, 196802 (2012).
- [13] K. F. Mak, K. He, J. Shan, and T. F. Heinz, *Nat. Nanotech.* **7**, 494 (2012).
- [14] A.-Y. Lu, H. Zhu, J. Xiao, C.-P. Chuu, Y. Han, M.-H. Chiu, C.-C. Cheng, C.-W. Yang, K.-H. Wei, Y. Yang, Y. Wang, D. Sokaras, D. Nordlund, P. Yang, D. A. Muller, M.-Y. Chou, X. Zhang, and L.-J. Li, *Nat. Nanotech.* **12**, 744 (2017).
- [15] J. Zhang, S. Jia, I. Kholmanov, L. Dong, D. Er, W. Chen, H. Guo, Z. Jin, V. B. Shenoy, L. Shi, and J. Lou, *ACS Nano* **11**, 8192 (2017).
- [16] M. A. U. Absor, I. Santoso, Harsojo, K. Abraha, H. Kotaka, F. Ishii, and M. Saito, *J. Appl. Phys.* **122**, 153905 (2017).
- [17] R. K. Defo, S. Fang, S. N. Shirodkar, G. A. Tritsarlis, A. Dimoulas, and E. Kaxiras, *Phys. Rev. B* **94**, 155310 (2016).
- [18] L. Dong, J. Lou, and V. B. Shenoy, *ACS Nano* **11**, 8242 (2017).
- [19] Y. C. Cheng, Z. Y. Zhu, M. Tahir, and U. Schwingenschlöggl, *Europhys. Lett.* **102**, 57001 (2013).
- [20] Q.-F. Yao, J. Cai, W.-Y. Tong, S.-J. Gong, J.-Q. Wang, X. Wan, C.-G. Duan, and J. H. Chu, *Phys. Rev. B* **95**, 165401 (2017).
- [21] C.-F. Fu, X. Li, Q. Luo, and J. Yang, *J. Mater. Chem. A* **5**, 24972 (2017).
- [22] A. Kudo and Y. Miseki, *Chem. Soc. Rev.* **38**, 253 (2009).
- [23] X. Li, Z. Li, and J. Yang, *Phys. Rev. Lett.* **112**, 018301 (2014).
- [24] Y. Ji, M. Yang, H. Dong, T. Hou, L. Wang, and Y. Li, *Nanoscale* **9**, 8608 (2017).
- [25] Y. Ji, M. Yang, H. Lin, T. Hou, L. Wang, Y. Li, and S.-T. Lee, *J. Phys. Chem. C* **122**, 3123 (2018).
- [26] G. Kresse and J. Furthmüller, *Phys. Rev. B* **54**, 11169 (1996).
- [27] P. E. Blöchl, *Phys. Rev. B* **50**, 17953 (1994).
- [28] J. P. Perdew, K. Burke, and M. Ernzerhof, *Phys. Rev. Lett.* **77**, 3865 (1996).
- [29] H. J. Monkhorst and J. D. Pack, *Phys. Rev. B* **13**, 5188 (1976).
- [30] S. Grimme, *J. Comput. Chem.* **27**, 1787 (2006).
- [31] T. Kerber, M. Sierka, and J. Sauer, *J. Comput. Chem.* **29**, 2088 (2008).
- [32] J. Heyd, J. E. Peralta, G. E. Scuseria, and R. L. Martin, *J. Chem. Phys.* **123**, 174101 (2005).
- [33] X. Gonze, J.-C. Charlier, D. C. Allan, and M. P. Teter, *Phys. Rev. B* **50**, 13035 (1994).
- [34] P. Giannozzi, S. de Gironcoli, P. Pavone, and S. Baroni, *Phys. Rev. B* **43**, 7231 (1991).
- [35] X. Gonze and C. Lee, *Phys. Rev. B* **55**, 10355 (1997).
- [36] J. D. Gale, *J. Chem. Soc., Faraday Trans.* **93**, 629 (1997).
- [37] J. D. Gale and A. L. Rohl, *Mol. Simul.* **29**, 291 (2003).
- [38] A. A. Mostofi, J. R. Yates, Y.-S. Lee, I. Souza, D. Vanderbilt, and N. Marzari, *Comput. Phys. Commun.* **178**, 685 (2008).
- [39] M. Rohlfling and S. G. Louie, *Phys. Rev. B* **62**, 4927 (2000).
- [40] M. Shishkin and G. Kresse, *Phys. Rev. B* **74**, 035101 (2006).
- [41] See Supplemental Material at <http://link.aps.org/supplemental/10.1103/PhysRevB.98.165424> for the relationship between structural parameters and atomic radius, molecular-dynamics simulation results of Janus *MXY*, phonon dispersion of monolayer MoS₂, band structures, band gaps, carrier mobilities, electrostatic potential of monolayer *MXY*, the specific structural parameters, electronic properties, and the potential energy difference with respect to the reduction and oxidation potential.
- [42] S. Tongay, J. Zhou, C. Ataca, K. Lo, T. S. Matthews, J. Li, J. C. Grossman, and J. Wu, *Nano Lett.* **12**, 5576 (2012).
- [43] C. Lee, H. Yan, L. E. Brus, T. F. Heinz, J. Hone, and S. Ryu, *ACS Nano* **4**, 2695 (2010).
- [44] A. Berkdemir, H. R. Gutiérrez, A. R. Botello-Méndez, N. Perea-López, A. L. Elías, C.-I. Chia, B. Wang, V. H. Crespi, F. López-Urías, J.-C. Charlier, H. Terrones, and M. Terrones, *Sci. Rep.* **3**, 1755 (2013).
- [45] W. Zhao, Z. Ghorannevis, K. K. Amara, J. R. Pang, M. Toh, X. Zhang, C. Kloc, P. H. Tan, and G. Eda, *Nanoscale* **5**, 9677 (2013).
- [46] I. G. Lezama, A. Arora, A. Ubaldini, C. Barreteau, E. Giannini, M. Potemski, and A. F. Morpurgo, *Nano Lett.* **15**, 2336 (2015).
- [47] B. Amin, T. P. Kaloni, and U. Schwingenschlöggl, *RSC Adv.* **4**, 34561 (2014).
- [48] Z. Wang, P. Liu, Y. Ito, S. Ning, Y. Tan, T. Fujita, A. Hirata, and M. Chen, *Sci. Rep.* **6**, 21536 (2016).
- [49] J.-S. Kim, R. Ahmad, T. Pandey, A. Rai, S. Feng, J. Yang, Z. Lin, M. Terrones, S. K. Banerjee, A. K. Singh, D. Akinwande, and J.-F. Lin, *2D Mater.* **5**, 015008 (2017).
- [50] Y. Sun, K. Fujisawa, Z. Lin, Y. Lei, J. S. Mondschein, M. Terrones, and R. E. Schaak, *J. Am. Chem. Soc.* **139**, 11096 (2017).
- [51] J. Nitta, T. Akazaki, H. Takayanagi, and T. Enoki, *Phys. Rev. Lett.* **78**, 1335 (1997).
- [52] A. D. Caviglia, M. Gabay, S. Gariglio, N. Reyren, C. Cancellieri, and J.-M. Triscone, *Phys. Rev. Lett.* **104**, 126803 (2010).
- [53] M. Z. Mayers, T. C. Berkelbach, M. S. Hybertsen, and D. R. Reichman, *Phys. Rev. B* **92**, 161404 (2015).
- [54] C. Zhang and Q. Sun, *J. Phys. Chem. Lett.* **7**, 2664 (2016).
- [55] M. M. Glazov, T. Amand, X. Marie, D. Lagarde, L. Bouet, and B. Urbaszek, *Phys. Rev. B* **89**, 201302 (2014).
- [56] L. Long, Y. Yang, H. Ye, and L. Wang, *J. Quant. Spectrosc. Radiat.* **200**, 198 (2017).
- [57] Z. Guan, C.-S. Lian, S. Hu, S. Ni, J. Li, and W. Duan, *J. Phys. Chem. C* **121**, 3654 (2017).
- [58] J. M. Bolts and M. S. Wrighton, *J. Phys. Chem.* **80**, 2641 (1976).
- [59] T. A. Pham, D. Lee, E. Schwegler, and G. Galli, *J. Am. Chem. Soc.* **136**, 17071 (2014).
- [60] X. Li, J. Yu, J. Low, Y. Fang, J. Xiao, and X. Chen, *J. Mater. Chem. A* **3**, 2485 (2015).